Nanosoldering Carbon Nanotube Junctions by Local Chemical Vapor Deposition for Improved Device Performance

Jae-Won Do,[†,⊥] David Estrada,[†,∥,¶] Xu Xie,[‡] Noel N. Chang,[§] Justin Mallek,[§] Gregory S. Girolami,[§,⊥] John A. Rogers,[‡,§,∥,⊥] Eric Pop,[†,∥,⊥,□] and Joseph W. Lyding*[,†,⊥]

[†]Department of Electrical and Computer Engineering, [‡]Department of Materials Science and Engineering and Frederick Seitz Materials Research Laboratory, [§]Department of Chemistry, [∥]Micro and Nanotechnology Laboratory, [⊥]Beckman Institute for Advanced Science and Technology, University of Illinois at Urbana—Champaign, Urbana, Illinois 61801, United States

Ⓢ Supporting Information

ABSTRACT: The performance of carbon nanotube network (CNN) devices is usually limited by the high resistance of individual nanotube junctions (NJs). We present a novel method to reduce this resistance through a nanoscale chemical vapor deposition (CVD) process. By passing current through the devices in the presence of a gaseous CVD precursor, localized nanoscale Joule heating induced at the NJs stimulates the selective and self-limiting deposition of metallic nano-solder. The effectiveness of this nanosoldering process depends on the work function of the deposited metal (here Pd or HfB_2), and it can improve the on/off current ratio of a CNN device by nearly an order of magnitude. This nanosoldering technique could also be applied to other device types where nanoscale resistance components limit overall device performance.

KEYWORDS: Carbon nanotubes (CNT), nanosoldering, intertube junctions, electrical resistance, thermal resistance, local chemical vapor deposition (CVD)
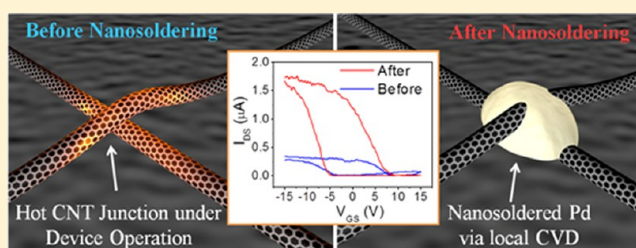
Single-walled carbon nanotubes (CNTs) can be thought of as one-dimensional cylinders of monolayer graphene. Semiconducting CNTs exhibit high carrier mobility[1,2] and band gaps which vary inversely with diameter,[3] whereas metallic CNTs can carry very high current densities.[4] These properties make CNTs promising candidates as components in nano-electronics.[5,6] However, as-grown CNTs are a mixture of metallic and semiconducting types, which often hinders their practical applications. For instance, such mixtures do not have sufficiently high on/off current (I_{ON}/I_{OFF}) ratios for low-power transistors, nor are they sufficiently metallic (i.e., independent of doping or gating) as interconnects. To address this challenge, there have been numerous attempts to eliminate metallic CNTs through electrical breakdown,[7,8] diazonium functionalization,[9,10] selective plasma etching,[6,11] or by polymer wrapping and CNT sorting through ultracentrifugation.[12] However, these methods require several postsynthesis process-ing steps that tend to contaminate or degrade the quality of the CNTs.

An alternative approach is to find ways to enhance the performance of random networks of as-grown carbon nanotube networks (CNNs). Such networks are easy to fabricate and transfer to arbitrary substrates, which make them attractive for applications in integrated circuits and display drivers on flexible or transparent substrates, especially because CNNs have shown higher carrier mobility than organic or amorphous silicon thin-film transistors.[13,14] Sun et al.[13] have recently improved the performance of CNN devices through control of the CNN

morphology and have achieved I_{ON}/I_{OFF} ratios of ~10^6 and carrier mobilities of ~20 cm^2 V^{-1} s^{-1}. One of the challenges associated with CNNs is that the performance and reliability may be limited by high electrical[15−19] and thermal[20−23] resistances of CNT−CNT internanotube junctions (NJs). Such resistances depend on the CNT−CNT separation and overlap, which affect the hopping probability of charge carriers and consequently the junction resistances.[18,19] From an electrical point of view, the current transport is further limited by Schottky barriers at the junctions between metallic and semiconducting CNTs.[24,25] These junction resistances are at least an order of magnitude higher than those of individual CNTs.[15−17] Thus, local power dissipation at these junctions will dramatically degrade the overall device performance.[21,26] To address this issue, several studies have sought to improve the junction resistance by depositing metal particles at the NJs using electron beam induced deposition[27] and dip-pen nanolithography facilitated by atomic force microscopy (AFM).[28] While elegant, these methods are slow, requiring one to locate individual junctions to deposit metal nano-particles in a serial fashion. Other studies have shown improvements in the sheet resistance of CNNs by employing selective nucleation of fullerenes at the NJs[29] and by treating CNNs with nitric acid and doping both the CNTs and the
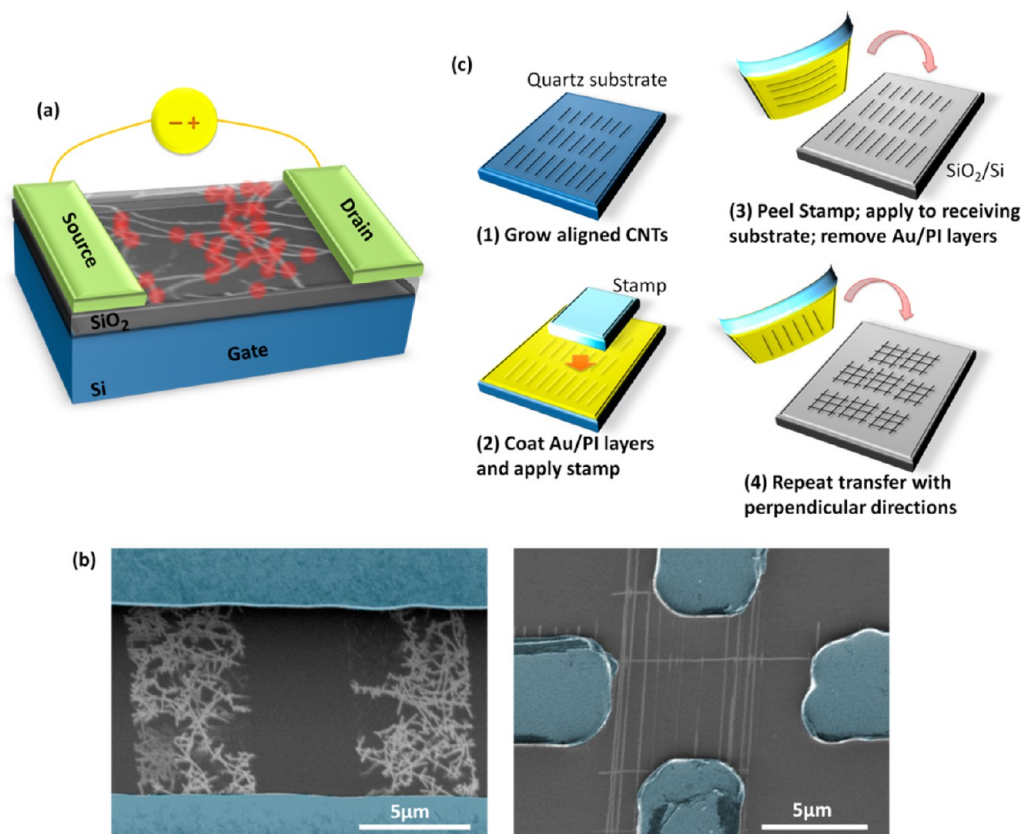
Figure 1. (a) Schematic diagram of a CNN device with red dots illustrating heated NJs under V_{DS}. (b) False-colored SEM images showing (left) CNNs bridging the drain and source electrodes and (right) crossbar CNT test device. (c) Schematic illustration of transferring aligned CNTs for crossbar devices as (1) aligned CNTs grown on quartz by CVD, followed by (2) deposition of a carrier film of Au and polyimide (PI) layers, and (3) applying an elastomeric stamp to transfer the resulting CNT/Au/PI layer to a receiving substrate, followed by removal of the stamp and Au/PI layer. The process is repeated (4) at orthogonal directions to achieve CNT arrays with crossbar orientation.

junctions.[30] However, the details of these improvements in terms of electronic properties specific to transistor applications, such as mobility and I_{ON}/I_{OFF} ratio, remained unexplored.

Recent transport studies of CNNs have shown that, during device operation, the temperature rise of the NJs is significantly higher than the average device temperature.[26,31] These findings indicate that nanoscale hot spots form at NJs throughout the CNN (Figure 1a), a conclusion that is supported by recent simulations.[32] In this study, we utilize these nanoscale hot spots to locally deposit metals via chemical vapor deposition (CVD). The net result is nanosoldering the NJs, which reduces their resistance and improves the overall CNN device performance.

We use test devices with two different geometries in our experiments, large area CNNs and CNT crossbar devices, as shown in Figure 1b. The CNNs were grown by CVD of methane gas with ferritin catalysts on SiO_2 (90 or 300 nm) with a highly doped Si substrate, which acts as a global back-gate.[26] For CNT crossbar devices, aligned CNTs were initially grown on quartz substrates by CVD methods described elsewhere[33,34] and subsequently transferred onto SiO_2 (200 nm) with a highly doped Si substrate at orthogonal directions to achieve well-defined NJs.[35,36] Figure 1c shows schematic illustrations of the preparation of the CNT crossbar devices. Standard photolithography and electron beam evaporation were used to define metal electrodes; the latter consisted of 0.5 nm Ti (an adhesion layer for the SiO_2 substrate) topped with 40−80 nm Pd, which forms ohmic contacts to CNTs, owing to its high work function and favorable interaction with CNT sidewalls.[37] Individual

devices were then wirebonded to metal leads of a chip carrier. Additional details about our device fabrication can be found in our previous papers[34,38,39] and in the Supporting Information.

In order to perform nanoscale CVD and nanosolder the NJs, entire samples were first loaded and kept in a vacuum chamber ($\sim 10^{-6}$ Torr or lower) for several hours. Figure 2a shows the process flow for nanosoldering the NJs and Figure 2b shows the schematic diagram of our vacuum system for the CVD reactions. The samples were vacuum annealed at 600 K for five minutes to desorb oxygen molecules from the CNTs and the metal electrodes.[40] (It is well-known that devices made of as-grown CNTs exhibit p-type behavior in air due to oxygen adsorption along the CNT and at the CNT−metal contacts.)[41,42] Oxygen removal lowers the contact work function,[41] causing conversion to n-type behavior in high vacuum.[40] This change for our devices before and after oxygen desorption is shown by the transfer characteristics (I_{DS} versus V_{GS} with V_{DS} = 50 mV) and band diagrams in Figure 2c. After the samples were vacuum annealed and cooled to room temperature, the individually wirebonded devices were additionally heated by applying various voltages between the source and drain electrodes, thereby passing currents through the CNT devices to desorb all remnant oxygen molecules. These additional heating steps were repeated until there was no discernible change in the transfer characteristics of the devices. The oxygen removal step is carried out in order to clearly observe any change in the current transport in our device that may arise from nanosoldering the NJs. After the transfer
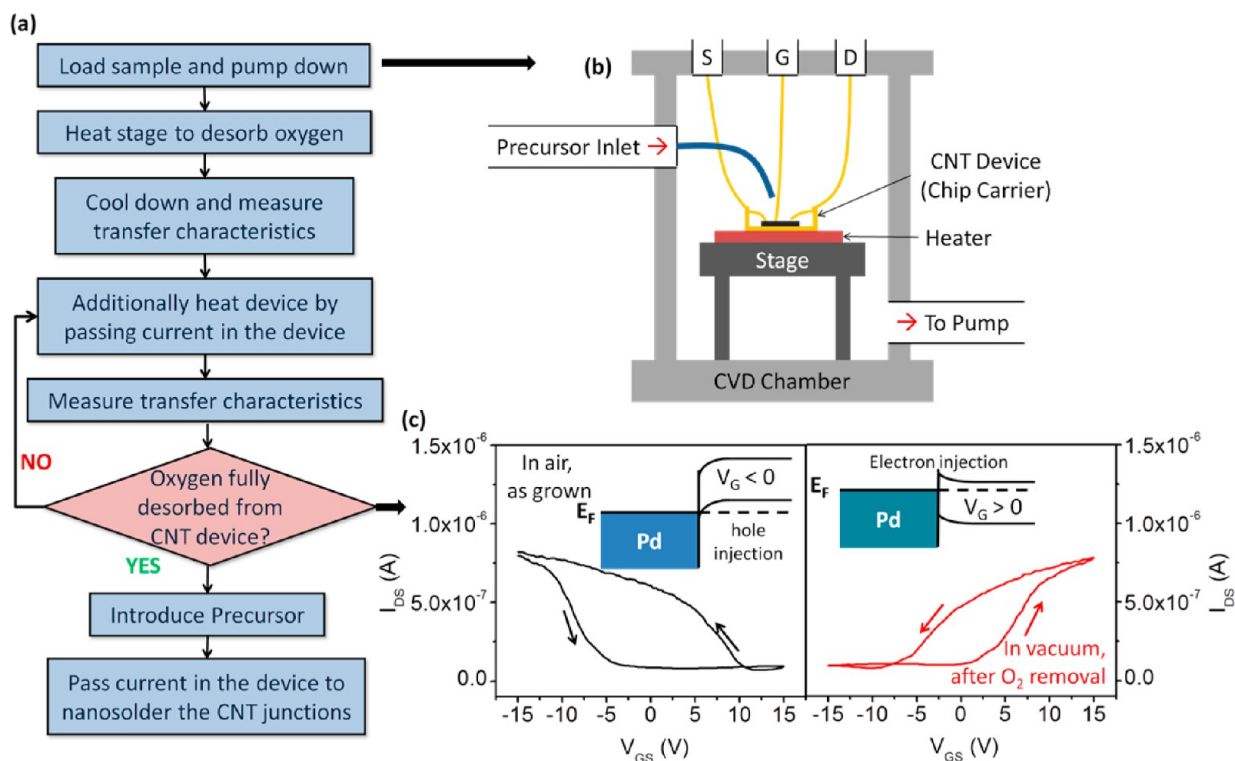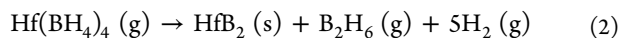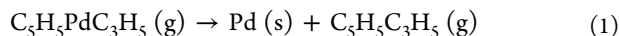
Figure 2. (a) Process flow for nanosoldering NJs. (b) Schematic diagram of vacuum system for our nanoscale CVD process. (c) Transfer characteristics of a CNN device (left) in air and (right) in vacuum after oxygen removal steps from the device. The arrows indicate the V_{GS} sweep direction. Corresponding energy band diagrams at the metal−CNT interface are shown in the insets of each graph. The left inset depicts hole injection into the CNT when a high work function metal, like Pd, contacts the CNT and the device is operated in air with $V_{GS} < 0$ V (p-type behavior). The right inset depicts electron injection into the CNT when the oxygen molecules are desorbed off from the metal surface and CNTs in vacuum and $V_{GS} > 0$ V is applied (n-type behavior).

characteristics stabilized, the background pressure of the CVD chamber was about $1-5 \times 10^{-6}$ Torr.

Once the pressure in the CVD chamber stabilized, a single-source CVD precursor, either $C_5H_5PdC_3H_5$ or $Hf(BH_4)_4$, was introduced into the chamber until a total pressure of about 10^{-4} Torr was achieved to deposit Pd and metallic HfB_2,[43,44] respectively. The approximate CVD reactions of each precursor are given by the following equations[43,45]

$$C_5H_5PdC_3H_5 \text{ (g)} \rightarrow Pd \text{ (s)} + C_5H_5C_3H_5 \text{ (g)} \quad (1)$$

$$Hf(BH_4)_4 \text{ (g)} \rightarrow HfB_2 \text{ (s)} + B_2H_6 \text{ (g)} + 5H_2 \text{ (g)} \quad (2)$$

Because the precursors are air sensitive, they were kept in sealed stainless steel and glass containers under argon and stored in an ice bath or in a refrigerator at -20 °C until use. Both precursors have relatively high-vapor pressures ($\sim$30 Torr at 25 °C for $C_5H_5PdC_3H_5$ and $\sim$15 Torr at 25 °C for $Hf(BH_4)_4$).[43,46]

After introduction of the precursors into the chamber, we varied the applied voltages over specific time periods to deposit Pd or HfB_2 at the locally heated NJs. Note that positive V_{GS} is used while varying V_{DS} in order to pass a high current because devices are now n-type. The I_{ON}/I_{OFF} ratios were subsequently measured to monitor changes resulting from metal deposition. Finally, the samples were removed from the vacuum system and exposed to the ambient atmosphere for sufficient time (over 24 h) to allow readsorption of oxygen molecules. The I_{ON}/I_{OFF} ratios were again measured to assess the effects of nanosoldering the NJs on the p-type characteristics of the devices. In order to calculate the I_{ON}/I_{OFF} ratio, we take I_{ON} at a constant

V_{GS} overdrive from the forward sweep ($V_{GS} - V_{TH,FWD} = -10$ V) and take I_{OFF} as the minimum I_{DS} from the same transfer curve (see Supporting Information) in order to better compare performance of different devices by comparing them at similar charge densities and to reduce variability due to V_{TH} shift.[47] Note that for devices with I_{OFF} lower than the measurement limit, the I_{OFF} was found by averaging currents in the regions with fluctuations in the off state below V_{TH}.

Figure 3a shows scanning electron microscope (SEM) images of a CNT crossbar device with well-defined NJs before and after Pd deposition. The two false-colored electrodes in red were used to pass current through the CNTs and electrodes in blue were left floating. V_{GS} was applied up to 15 V in order to "turn on" both metallic and semiconducting CNTs, and V_{DS} was applied from 5 to 35 V for three seconds. Figure 3b shows the transfer characteristic curves before and after Pd deposition for the device shown in Figure 3a. These results indicate that the I_{ON} was improved by a factor of $\sim$6, while the I_{OFF} (averaged in the regions indicated by black arrows) was lowered by a factor of $\sim$1.42, leading to I_{ON}/I_{OFF} ratio improvement by a factor of $\sim$8.52. We also note that there was no significant effect on the threshold voltage hysteresis ($\Delta V_{TH,FWD} - V_{TH,REV} = 0.015$ V), suggesting that Pd nanosoldering does not introduce new trap states near the CNT-SiO$_2$ interface.[2] Thus, if we assume the current paths between source and drain electrodes remain unchanged (at a constant V_{GS} overdrive) before and after Pd deposition, the improvement in I_{ON} is indicative of an increase in the average device mobility by a factor of $\sim$6. Please refer to Figure S2b in
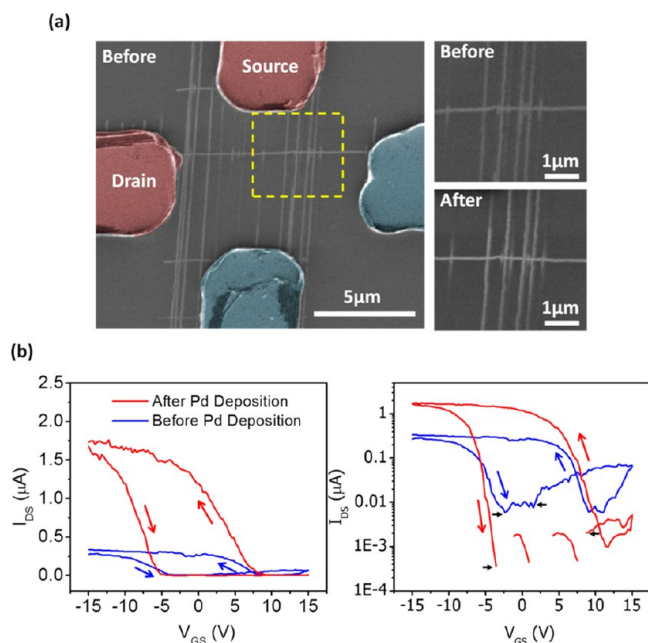
Figure 3. (a) (Left) SEM image of crossbar CNT device before Pd deposition where current was passed between the two false-colored red electrodes to heat the NJs. Blue electrodes were left floating. (Right) Zoomed-in NJs indicated by yellow dotted box in the left image (top) before and (bottom) after Pd deposition showing traces of Pd along CNTs near the NJs. (b) (Left) linear and (right) log scale transfer characteristics of the CNN device before and after Pd deposition with $V_{DS} = 1$ V. The red and blue arrows indicate the V_{GS} sweep direction. Note that the I_{OFF} was found by averaging the current in the regions indicated by black arrows. Please refer to Figure S2b in the Supporting Information for n-type transfer characteristic curves in vacuum.

Figure 4. Energy band diagrams at the metal−CNT interface showing (a) (top) back-to-back p-type junctions when high work function metal, like Pd, is used to connect two semiconducting CNTs at a NJ with Pd electrodes and (bottom) back-to-back pnp junctions when low work function metal, like HfB$_2$, is used to connect CNTs. (b) Energy band diagrams when (top) Pd and (bottom) HfB$_2$ are used to connect two metallic CNTs at a junction. (c) Energy band diagrams showing (top) p-type junction when Pd is used to connect metallic and semiconducting CNTs at a NJ and (bottom) pn junction when HfB$_2$ is used to connect CNTs.

the Supporting Information for n-type transfer characteristic curves in vacuum.

We attribute the increase in I_{ON} to higher charge carrier hopping probability at the NJs, and thus lowered junction resistance. As Pd is deposited at the NJs, the area available for carrier flow is increased and the energy barrier is lowered. The decrease in I_{OFF} may result from a heightened Schottky barrier for electrons in the off state. Figure 4 shows the schematic band diagrams for nanosoldered NJs between semiconducting CNTs, metallic CNTs, and semiconducting-metallic CNTs. In the devices we studied, Pd is used for both the source and drain electrodes, and the CNTs form percolation paths between the two electrodes. CNT contacts to Pd electrodes induce p-type behavior at the source and drain because Pd has a high work function ($\Phi_{PD} = 5.1-5.9$ eV.)[48−50] Therefore, nanosoldering the NJs with Pd will also induce p-type behavior at these NJs, and the lowered Schottky barrier at the valence band edge and increased Schottky barrier for electrons in the off state will lead to a large improvement in the overall device performance. We note that even though a large improvement in the I_{ON}/I_{OFF} ratio was observed, we did not find any large Pd particles after nanosoldering (see Figure 3a). Instead, a slight increase in contrast along some CNTs near the NJs was observed after Pd deposition as can be seen in Figure 3a. The right-hand images are magnified views of the region indicated by the yellow dotted box, before and after Pd deposition. We speculate that only a very small amount of Pd is needed to connect the CNTs at the NJs because Pd is known to wet CNTs very well.[51,52] Once
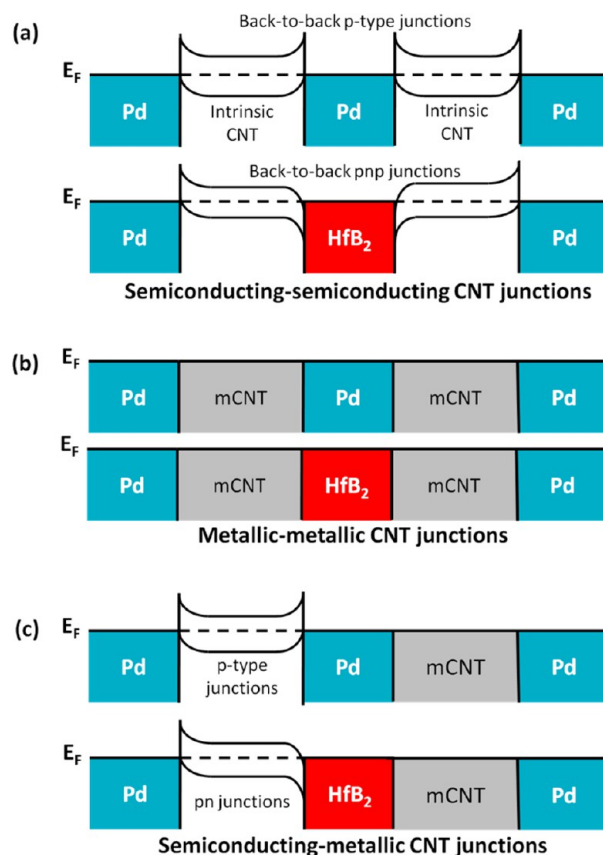
these NJs are soldered, their resistance decreases and they cool, thus stopping the nanosoldering process.

In order to confirm that Pd was deposited on the NJs, the nanosoldering was deliberately carried out with high currents for longer times (up to 30 s) on other similar devices to deposit a larger amount of Pd. Post characterization with SEM and AFM (see Figure S5 in Supporting Information) indicate that Pd nanoparticles from sub-10 nm to over 30 nm in size were deposited on the NJs. The deposited material was also verified to be Pd by elemental analysis using energy dispersive X-ray spectroscopy (EDS).

Additional control experiments were performed on similar crossbar and CNN devices that were annealed in vacuum and subjected to the similar set of deposition conditions without actually introducing any precursor into the chamber. These experiments allowed us to test the possibility that the improvement in device performance was due to factors other than nanosoldering. For a majority of devices we tested, the $I_{DS}-V_{GS}$ characteristics remained about the same or even degraded after these control experiments (see Supporting Information). On a single device, we saw an I_{ON}/I_{OFF} ratio improvement of a factor of ~2.4, possibly due to the elimination of contaminants on CNTs or thermal annealing

of the contacts from the heat generated during current flow. However, we were able to nanosolder this same device with Pd after the control experiment and improve the I_{ON} by a factor of ~5.9 while decreasing the I_{OFF} by a factor of ~1.4, leading to the overall performance improvement of another factor of ~8.25 (see Supporting Information). Notably, we have not observed any device for which I_{OFF} decreases after a control experiment conducted without the CVD precursor. Thus the decreased I_{OFF} after Pd deposition in our devices suggests that nanosoldering Pd is indeed playing a role at the NJs. In order to test the stability of the improved junctions with time, we also performed time-dependence measurements in which current was passed through one of our nanosoldered devices for more than 20 h (see Figure S3 in Supporting Information). The stable current during the device operation and consistent transfer curves in Supporting Information Figure S3 show that our technique does not suffer from stability issues such as electromigration or oxidation.

In order to clarify the effect of the nanosolder work function, we then used the precursor $Hf(BH_4)_4$ to deposit HfB_2 at the NJs. We chose the precursor $Hf(BH_4)_4$ because the resultant HfB_2 has a high melting point (3250 °C) and excellent electrical properties:[43] a resistivity of ~15 $\mu\Omega\cdot$cm and a low work function ($\Phi_{HfB2} \approx 3.5$ eV).[53] Figure 5a shows SEM images of a CNN device before and after HfB_2 nanosoldering. The bright islands in the figure indicate that HfB_2 has been deposited primarily at crossed NJs. We also note that a few
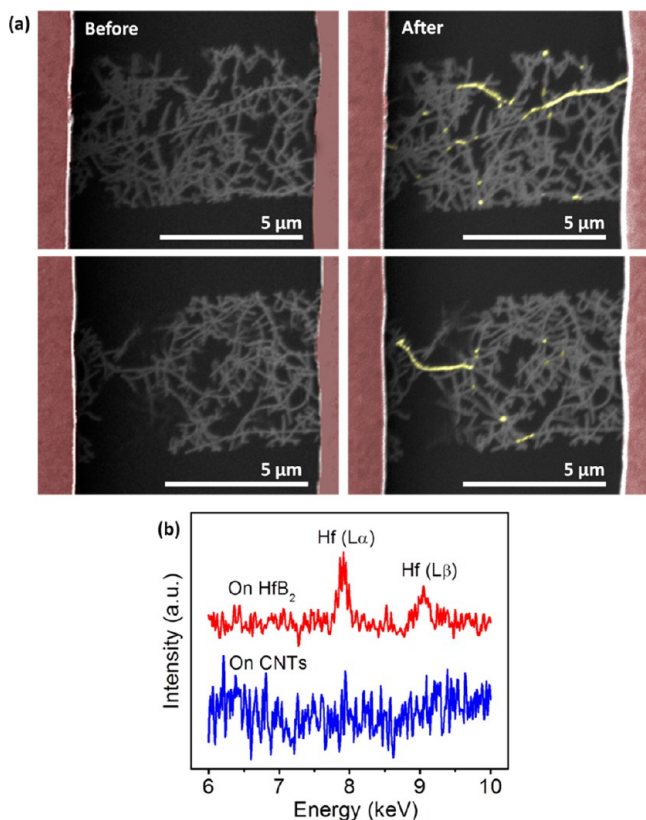

Figure 5. (a) SEM images of CNNs (left) before and (right) after nano-CVD of HfB_2. The drain and source electrodes are false-colored in red and the deposited HfB_2 is false-colored in yellow. (b) Energy dispersive X-ray spectroscopy (EDS) spectra from HfB_2 deposited on NJs (red) and on CNTs in the same device where no HfB_2 was deposited (blue).

CNTs are coated with HfB_2 along almost their entire lengths, vividly highlighting the most conductive current pathways that heat up during device operation. EDS measurements confirm the presence of hafnium: the red curve in Figure 5b shows the EDS spectrum obtained from a bright island formed at a NJ, whereas the blue curve shows the EDS spectrum obtained from CNTs in the same device away from the bright island under the same acquisition conditions. Data regarding the presence of boron are provided in the Supporting Information.

Figure 6a shows SEM images of another CNN device before and after HfB_2 deposition. The yellow circles indicate regions where HfB_2 was deposited on the NJs. Figure 6b shows the transfer characteristics of this device before and after HfB_2 deposition where the I_{ON}/I_{OFF} ratio was improved by ~24% using our nanosoldering technique. Note that there was little change on the threshold voltage hysteresis ($\Delta V_{TH,FWD} - V_{TH,REV} = 0.23$ V), suggesting that HfB_2 nanosoldering does not introduce new trap states.[2] We tested several other devices with similar channel geometries, as well as CNT crossbar devices, and found the device performance either showed less improvement or could even be degraded (see Supporting Information for more data). We believe that the difference in the work function of the electrode metal, Pd, and the deposited metal, HfB_2, plays a role here. When a low work function metal comes in contact with a semiconducting CNT, charge transfer occurs from the metal to the CNT and creates a Schottky barrier at the valence band edge, inducing n-type behavior at the contact as shown in Figure 4. Therefore, when the NJs are nanosoldered with HfB_2, n-type behavior is induced in the middle of the CNT percolation paths between the source and drain electrodes, while p-type behavior is induced at CNT contacts to the source and drain electrodes because Pd has a high work function. This mismatch of work functions will create back-to-back pnp junctions within the CNN for HfB_2 nanosoldered junctions, which can degrade the current transport of the device. We also note that, unlike the Pd case, large HfB_2 particles were visible after nanosoldering the junctions (see Figures 5 and 6). We believe that when HfB_2 is deposited at these NJs, the resistance will not drop as much due to the work function mismatch and the poor interface between HfB_2 and CNTs (compared to Pd which wets CNTs very well) and thus the nanosoldering process will continue, making much larger islands. Figure 6c shows a histogram that summarizes the degree of improvement in the I_{ON}/I_{OFF} ratio ($I_{ON}/I_{OFF,AFTER}/I_{ON}/I_{OFF,BEFORE}$) for the control, HfB_2-deposited, and Pd-deposited devices. For more details on these devices, please refer to Figure S4 in Supporting Information.

In conclusion, we achieved nanoscale CVD of metallic nanoparticles at NJs by passing current through devices like CNNs and CNT crossbars to selectively heat the NJs. This process results in self-aligned and self-limiting nanosoldering that reduces the junction resistance and improves the device transport properties. By matching the work function of the electrode with the metallic nanosolder (e.g., by using Pd), we improved the I_{ON}/I_{OFF} ratio of our devices by nearly an order of magnitude. The self-limiting nature of the nanosoldering process means that the NJs cool as they are soldered, and the next most-resistive NJs will undergo nanosoldering. The nanosoldering technique may be generally applicable to improve the performance of other materials and devices.
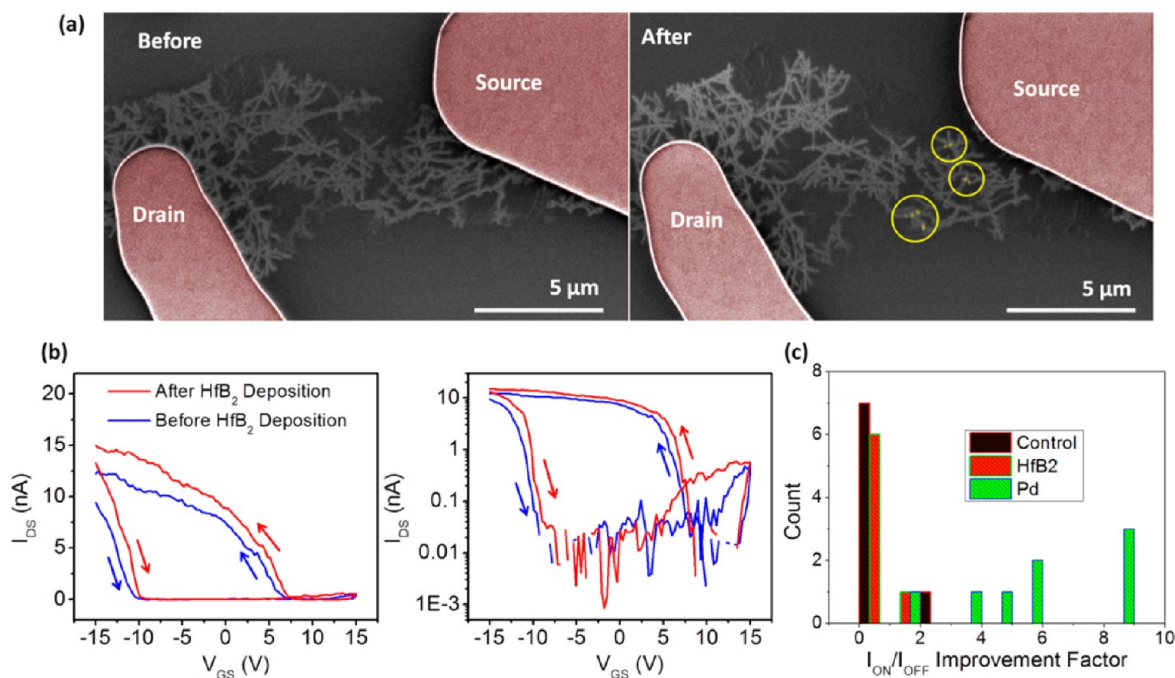
Figure 6. (a) False-colored SEM images of a CNN before (left) and after (right) HfB_2 deposition. Yellow circles are used to indicate NJs where HfB_2 was deposited. (b) Linear (left) and log (right) scale transfer characteristics of the CNN device before and after HfB_2 deposition with $V_{DS} = 50$ mV. The arrows indicate V_{GS} sweep direction. Note that the measurement in (b) was made before SEM imaging and the breaking of CNTs near the source in (a) was caused by electrostatic discharge during handling after the measurement. (c) A histogram showing the improvement in I_{ON}/I_{OFF} ratios upon control experiment (black), HfB_2 deposition (red), and Pd deposition (green).

ASSOCIATED CONTENT

Ⓢ Supporting Information

We include fabrication of CNT devices, sample preparation and experimental setup, control experiments and additional data analysis on reliability and vacuum measurements, verification of Pd deposition on CNTs, and energy dispersive spectroscopy (EDS) data for boron. This material is available free of charge via the Internet at http://pubs.acs.org.

AUTHOR INFORMATION

Corresponding Author

*E-mail: lyding@illinois.edu.

Present Addresses

¶Department of Materials Science and Engineering, Boise State University, Boise, ID 83725, U.S.A.
□Department of Electrical Engineering, Stanford University, Stanford, CA 94305, U.S.A.

Notes

The authors declare no competing financial interest.

ACKNOWLEDGMENTS

REFERENCES

(1) Zhou, X.; Park, J.-Y.; Huang, S.; Liu, J.; McEuen, P. *Phys. Rev. Lett.* **2005**, *95*, 1−4.

(2) Estrada, D.; Dutta, S.; Liao, A.; Pop, E. *Nanotechnology* **2010**, *21*, 85702.

(3) Park, J.-Y. Band Structure and Electron Transport Physics of One-Dimensional SWNTs. In *Carbon Nanotube Electronics*; Javey, A., Kong, J., Eds.; Integrated Circuits and Systems; Springer: New York, 2009; pp 1−42.

(4) Liao, A.; Alizadegan, R.; Ong, Z.-Y.; Dutta, S.; Xiong, F.; Hsia, K. J.; Pop, E. *Phys. Rev. B: Condens. Matter Mater. Phys.* **2010**, *82*, 205406.

(5) Cao, Q.; Han, S.; Tulevski, G. S.; Zhu, Y.; Lu, D. D.; Haensch, W. *Nat. Nanotechnol.* **2013**, *8*, 180−186.

(6) Jin, S. H.; Dunham, S. N.; Song, J.; Xie, X.; Kim, J.-H.; Lu, C.; Islam, A.; Du, F.; Kim, J.; Felts, J.; Li, Y.; Xiong, F.; Wahab, M. A.; Menon, M.; Cho, E.; Grosse, K. L.; Lee, D. J.; Chung, H. U.; Pop, E.; Alam, M. A.; King, W. P.; Huang, Y.; Rogers, J. A. *Nat. Nanotechnol.* **2013**, *8*, 347−355.

(7) Collins, P. G.; Arnold, M. S.; Avouris, P. *Science* **2001**, *292*, 706−709.

(8) Seidel, R.; Graham, A. P.; Unger, E.; Duesberg, G. S.; Liebau, M.; Steinhoegl, W.; Kreupl, F.; Hoenlein, W.; Pompe, W. *Nano Lett.* **2004**, *4*, 831−834.

(9) Strano, M. S.; Dyke, C. A.; Usrey, M. L.; Barone, P. W.; Allen, M. J.; Shan, H.; Kittrell, C.; Hauge, R. H.; Tour, J. M.; Smalley, R. E. *Science* **2003**, *301*, 1519−1522.

(10) Schmidt, G.; Filoramo, A.; Derycke, V.; Bourgoin, J.-P.; Chenevier, P. *Chem.—Eur. J.* **2011**, *17*, 1415−1418.

(11) Zhang, G.; Qi, P.; Wang, X.; Lu, Y.; Li, X.; Tu, R.; Bangsaruntip, S.; Mann, D.; Zhang, L.; Dai, H. *Science* **2006**, *314*, 974−977.

(12) Lee, H. W.; Yoon, Y.; Park, S.; Oh, J. H.; Hong, S.; Liyanage, L. S.; Wang, H.; Morishita, S.; Patil, N.; Park, Y. J.; Park, J. J.; Spakowitz, A.; Galli, G.; Gygi, F.; Wong, P. H.-S.; Tok, J. B.-H.; Kim, J. M.; Bao, Z. *Nat. Commun.* **2011**, *2*, 541.

(13) Sun, D.; Timmermans, M. Y.; Tian, Y.; Nasibulin, A. G.; Kauppinen, E. I.; Kishimoto, S.; Mizutani, T.; Ohno, Y. *Nat. Nanotechnol.* **2011**, *6*, 156−161.

(14) Cao, Q.; Kim, H.; Pimparkar, N.; Kulkarni, J. P.; Wang, C.; Shim, M.; Roy, K.; Alam, M. A.; Rogers, J. A. *Nature* **2008**, *454*, 495−500.

(15) Hu, L.; Hecht, D. S.; Grüner, G. *Nano Lett.* **2004**, *4*, 2513−2517.

(16) Nirmalraj, P. N.; Lyons, P. E.; De, S.; Coleman, J. N.; Boland, J. J. *Nano Lett.* **2009**, *9*, 3890−3895.

(17) Stadermann, M.; Papadakis, S.; Falvo, M.; Novak, J.; Snow, E.; Fu, Q.; Liu, J.; Fridman, Y.; Boland, J.; Superfine, R.; Washburn, S. *Phys. Rev. B: Condens. Matter Mater. Phys.* **2004**, *69*, 201402.

(18) Alam, M. A.; Pimparkar, N.; Kumar, S.; Murthy, J. *MRS Bull.* **2006**, *31*, 466−470.

(19) Kyrylyuk, A. V; Hermant, M. C.; Schilling, T.; Klumperman, B.; Koning, C. E.; Van der Schoot, P. *Nat. Nanotechnol.* **2011**, *6*, 364−369.

(20) Kumar, S.; Alam, M. A.; Murthy, J. Y. *Appl. Phys. Lett.* **2007**, *90*, 104105.

(21) Zhong, H.; Lukes, J. *Phys. Rev. B: Condens. Matter Mater. Phys.* **2006**, *74*, 125403.

(22) Prasher, R.; Hu, X.; Chalopin, Y.; Mingo, N.; Lofgreen, K.; Volz, S.; Cleri, F.; Keblinski, P. *Phys. Rev. Lett.* **2009**, *102*, 105901.

(23) Yang, J.; Waltermire, S.; Chen, Y.; Zinn, A. A.; Xu, T. T.; Li, D. *Appl. Phys. Lett.* **2010**, *96*, 023109.

(24) Yao, Z.; Postma, H. W. C.; Balents, L.; Dekker, C. *Nature* **1999**, *402*, 273−276.

(25) Fuhrer, M. S. *Science* **2000**, *288*, 494−497.

(26) Estrada, D.; Pop, E. *Appl. Phys. Lett.* **2011**, *98*, 073102.

(27) Wang, M. S.; Wang, J. Y.; Chen, Q.; Peng, L.-M. *Adv. Funct. Mater.* **2005**, *15*, 1825−1831.

(28) Shen, G.; Lu, Y.; Shen, L.; Zhang, Y.; Guo, S. *ChemPhysChem* **2009**, *10*, 2226−2229.

(29) Virkar, A. In *Investigating the Nucleation, Growth, and Energy Levels of Organic Semiconductors for High Performance Plastic Electronics*; Springer: New York, 2012; pp 115−128.

(30) Znidarsic, A.; Kaskela, A.; Laiho, P.; Gaberscek, M.; Ohno, Y.; Nasibulin, A. G.; Kauppinen, E.; Hassanien, A. *J. Phys. Chem. C* **2013**, *117*, 13324−13330.

(31) Behnam, A.; Sangwan, V. K.; Zhong, X.; Lian, F.; Estrada, D.; Jariwala, D.; Hoag, A. J.; Lauhon, L. J.; Marks, T. J.; Hersam, M. C.; Pop, E. *ACS Nano* **2013**, *7*, 482−490.

(32) Gupta, P. M.; Chen, L.; Estrada, D.; Behnam, A.; Pop, E.; Kumar, S. *J. Appl. Phys.* **2012**, *112*, 124506.

(33) Kang, S. J.; Kocabas, C.; Ozel, T.; Shim, M.; Pimparkar, N.; Alam, M. A.; Rotkin, S. V; Rogers, J. A. *Nat. Nanotechnol.* **2007**, *2*, 230−236.

(34) Xiao, J.; Dunham, S.; Liu, P.; Zhang, Y.; Kocabas, C.; Moh, L.; Huang, Y.; Hwang, K.-C.; Lu, C.; Huang, W.; Rogers, J. A. *Nano Lett.* **2009**, *9*, 4311−4319.

(35) Kang, S. J.; Kocabas, C.; Kim, H.-S.; Cao, Q.; Meitl, M. A.; Khang, D.-Y.; Rogers, J. A. *Nano Lett.* **2007**, *7*, 3343−3348.

(36) Tsai, C.-L.; Xiong, F.; Pop, E.; Shim, M. *ACS Nano* **2013**, *7*, 5360−5366.

(37) Javey, A.; Guo, J.; Wang, Q.; Lundstrom, M.; Dai, H. *Nature* **2003**, *424*, 654−657.

(38) Hur, S.-H.; Kocabas, C.; Gaur, A.; Park, O. O.; Shim, M.; Rogers, J. A. *J. Appl. Phys.* **2005**, *98*, 114302.

(39) Do, J.-W.; Estrada, D.; Chang, N.; Girolami, G. S.; Rogers, J. A.; Pop, E.; Lyding, J. W. Nanosoldering Carbon Nanotube Junctions with Metal via Local Chemical Vapor Deposition for Improved Device Performance. In *2012 12th IEEE International Conference on Nanotechnology (IEEE-NANO)*, Birmingham, U.K., Aug 20−23, 2012; IEEE: New York, 2012; 8325.

(40) Derycke, V.; Martel, R.; Appenzeller, J.; Avouris, P. *Appl. Phys. Lett.* **2002**, *80*, 2773−2775.

(41) Huang, W.; Zhai, R.; Bao, X. *Appl. Surf. Sci.* **2000**, *158*, 287−291.

(42) Cui, X.; Freitag, M.; Martel, R.; Brus, L.; Avouris, P. *Nano Lett.* **2003**, *3*, 783−787.

(43) Jayaraman, S.; Yang, Y.; Kim, D. Y.; Girolami, G. S.; Abelson, J. R. *J. Vac. Sci. Technol., A* **2005**, *23*, 1619−1625.

(44) Gozum, J. E.; Pollina, D. M.; Jensen, J. A.; Girolami, G. S. *J. Am. Chem. Soc.* **1988**, *110*, 2688−2689.

(45) Hierso, J.-C.; Serp, P.; Feurer, R.; Kalck, P. *Appl. Organomet. Chem.* **1998**, *12*, 161−172.

(46) Tatsuno, Y.; Yoshida, T.; Otsuka, S.; Al-Salem, N.; Shaw, B. L. In *Inorganic Syntheses*; Shriver, D. F., Ed.; John Wiley & Sons, Inc.: Hoboken, NJ, 2007; Vol. *19*, pp 220−223.

(47) Timmermans, M. Y.; Estrada, D.; Nasibulin, A. G.; Wood, J. D.; Behnam, A.; Sun, D.; Ohno, Y.; Lyding, J. W.; Hassanien, A.; Pop, E.; Kauppinen, E. I. *Nano Res.* **2012**, *5*, 307−319.

(48) Gu, D.; Dey, S. K.; Majhi, P. *Appl. Phys. Lett.* **2006**, *89*, 082907.

(49) Skriver, H.; Rosengaard, N. *Phys. Rev. B: Condens. Matter Mater. Phys.* **1992**, *46*, 7157−7168.

(50) Wandelt, K. In *Thin Metal Films and Gas Chemisorption*; Wissman, P., Ed.; Elsevier Science: Amsterdam, 1987; Vol. *32*, pp 280−363.

(51) Zhang, Y.; Franklin, N. W.; Chen, R. J.; Dai, H. *Chem. Phys. Lett.* **2000**, *331*, 35−41.

(52) Zhang, Y.; Dai, H. *Appl. Phys. Lett.* **2000**, *77*, 3015.

(53) Samsonov, G. V.; Fomenko, V. S.; Kunitskii, Y. A. *Russ. Phys. J.* **1972**, *15*, 502−505.

Nanosoldering Carbon Nanotube Junctions by Local Chemical Vapor Deposition for Improved Device Performance

Jae-Won Do,[1,5] David Estrada,[1,4,6] Xu Xie,[2] Noel N. Chang,[3] Justin Mallek,[3] Gregory S. Girolami,[3,5] John A. Rogers,[2,3,4,5] Eric Pop,[1,4,5,7] Joseph W. Lyding[1,5*]

[1]Department of Electrical and Computer Engineering,
[2]Department of Materials Science and Engineering and Frederick Seitz Materials Research Laboratory,
[3]Department of Chemistry,
[4]Micro and Nanotechnology Laboratory,
[5]Beckman Institute for Advanced Science and Technology,
University of Illinois at Urbana-Champaign, Urbana, IL 61801, USA.
[6]Present Address: Department of Materials Science and Engineering, Boise State University, Boise, ID 83725, USA.
[7]Present Address: Department of Electrical Engineering, Stanford University, Stanford, CA 94305, USA.

[*]Corresponding author. E-mail: lyding@illinois.edu

Table of Contents:

1. Fabrication of Carbon Nanotube (CNT) Devices

CNT devices of two different geometries (network and crossbar) were prepared for our experiments. The carbon nanotube networks (CNN) were grown by chemical vapor deposition (CVD) using CH_4 gas as the carbon feedstock and H_2 as the carrier gas at 900 °C.[1] Ferritin (Sigma-Aldrich) catalyst was diluted in deionized water and spincast on thermally grown 90 nm and 300 nm SiO_2 films on highly doped silicon substrates, which were used as backgates. Prior to CNT growth, the catalyst was oxidized by heating the wafer to 900 ºC, and cooled to room temperature in an air environment. The wafer was heated to 900 °C again with H_2 to reduce the catalyst, and CNTs were grown at 900 °C for 15 minutes under CH_4 and H_2 flows.

The CNTs for crossbar devices were grown by CVD using Ar and H_2, bubbled through chilled (0 °C) ethanol at 925 °C for 20 minutes.[2] For catalyst, a solution of ferritin diluted in deionized water was spincast onto a stable temperature (ST) cut quartz substrate to grow aligned CNTs. In order to achieve crossbar configuration, double transfer of CNTs was performed[3] to thermally grown 200 nm SiO_2 films on highly doped silicon substrates, which were used as backgates. The transfer process involved depositing a thin carrier layer of Au and polyimide (PI) onto the CNTs, and peeling and transferring the carrier layer along with CNTs using an elastomeric stamp of polydimethylsiloxane (PDMS). After transferring CNTs to target substrates, the carrier layer was removed by oxygen reactive ion etching (RIE) and wet etching with a commercial solution (Au-TFA, Transene). This transfer process was repeated in orthogonal directions to achieve the crossbar configuration. Finally, the CNTs were patterned by standard photolithography and O_2 plasma etching. For electrodes, 40 nm to 80 nm of Pd was evaporated with a thin layer of Ti (0.5 nm) to improve the adhesion to the SiO_2 film, and patterned by lift-off. See Figure 1 in the main text for images of completed devices.

2. Device Preparation and Experimental Setup

After fabricating CNT devices, individual devices were wirebonded to the metal leads of a chip carrier using a 4524 Au Wire Ball Bonder (K&S). Figure S1a shows optical images of our wafer on a chip carrier with the inset image showing a zoomed-in view of CNT devices after wirebonding. Figure S1b shows a scanning electron microscope (SEM) image of one of our wirebonded CNT devices. SEM images were collected using Philips XL30 ESEM-FEG at an operating voltage of 1 kV.
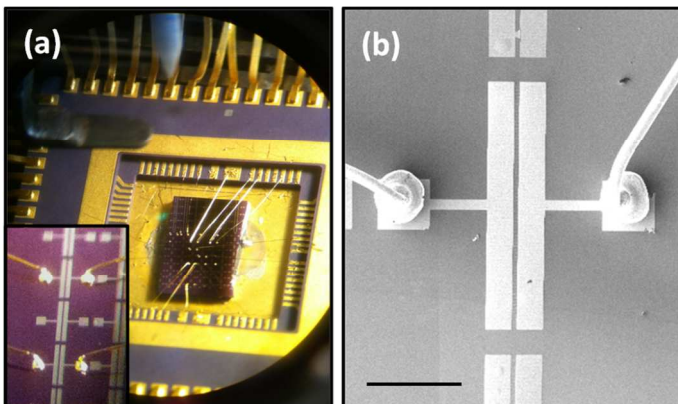

Figure S1. (a) Optical images of carbon nanotube (CNT) devices on a chip carrier after wirebonding. **(b)** Scanning electron microscope (SEM) image of a wirebonded CNT device. Scale bar is 200 µm.

The precursor compounds, $Hf(BH_4)_4$ and $C_5H_5PdC_3H_5$ (CpPd(allyl)), were synthesized by methods described elsewhere.[4,5] The gas delivery system to our home-built CVD chamber (see Figure 2b in the main text for a schematic diagram) consists of precursor reservoirs, two leak valves, and a stainless steel capillary doser. The flow was regulated by the leak valves and delivered to the sample through a stainless steel tube pointing directly at the CNT devices at a distance of about 2 cm. Prior to the CVD experiments, the precursors were kept in sealed stainless steel and glass containers under argon and stored in a refrigerator at -20 °C. For the actual experiments, the precursors were maintained at either 0 °C in an ice-water bath or at room temperature in order to achieve total pressure of $\sim10^{-4}$ Torr in the CVD chamber.

3. <u>More Data Analysis and Control Experiments</u>

All dc electrical characterizations in our experiments were performed with an HP 4155A semiconductor parameter analyzer. As noted in the main text, we use I_{ON} at a constant V_{GS} overdrive from the forward sweep ($V_{GS} - V_{TH,FWD}$ = -10 V) and take I_{OFF} as the minimum I_{DS} from the same transfer curve to calculate the I_{ON}/I_{OFF} ratio. For devices with $V_{TH,FWD} < $ -5 V, I_{DS} at V_{GS} = -15 V is used as I_{ON}, and the constant V_{GS} overdrive between V_{GS} = -15V and $V_{TH,FWD}$ is used for both before and after metal deposition cases. This approach compares all devices at similar charge densities and reduces variability due to V_{TH} shift, and thus allows for a better comparison of performance across different devices.[6] For devices with I_{OFF} lower than the measurement limit, the I_{OFF} was found by averaging currents in the regions with fluctuations in the off state below V_{TH}.

In order to test the stability of the improved junctions with time, we measured the transfer characteristics of our devices after operating them in air. The blue curve in Figure S2a shows the transfer curve after the device was exposed to air for two days. After another day, current was passed to this device with V_{DS} = 5 V and V_{GS} = -15 V for 10 seconds and the transfer characteristics was measured again (see red curve). We have noticed no noticeable difference between the two measurements, and used only the black and red curves in the main text in Figure 3b as before and after nanosoldering experiment data. Figure S2b shows how this device was converted to n-type after oxygen removal in vacuum, and how the performance was improved by nanosoldering while the device remained in vacuum.
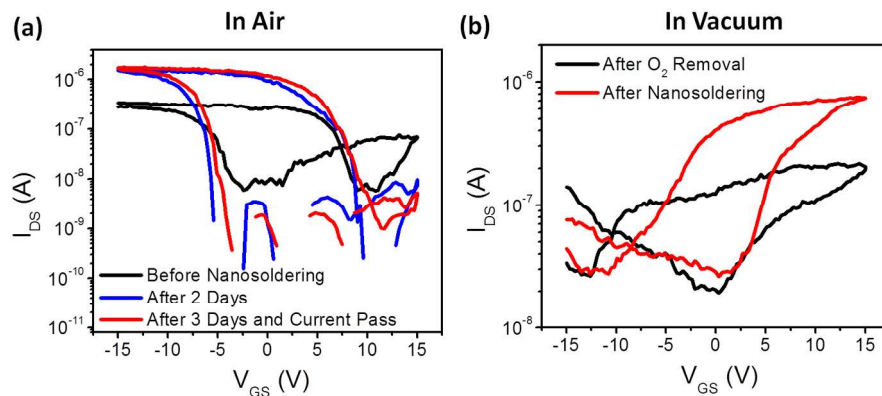

Figure S2. (a) In-air transfer characteristics of the device in Figure 3a in the main text. **(b)** In-vacuum transfer characteristics of the device in Figure 3a in the main text.

To further test the stability of our nanosoldering technique, current was passed to one of our nanosoldered devices for more than 20 hours. Figure S3 shows the current throughout the time period the device was under operation, and the inset plots show 10 transfer characteristic curves measured before and after the 20-hour current pass. The stable current during the device operation and consistent transfer curves show that our technique does not cause any stability issues related to possible electromigration and oxidation.
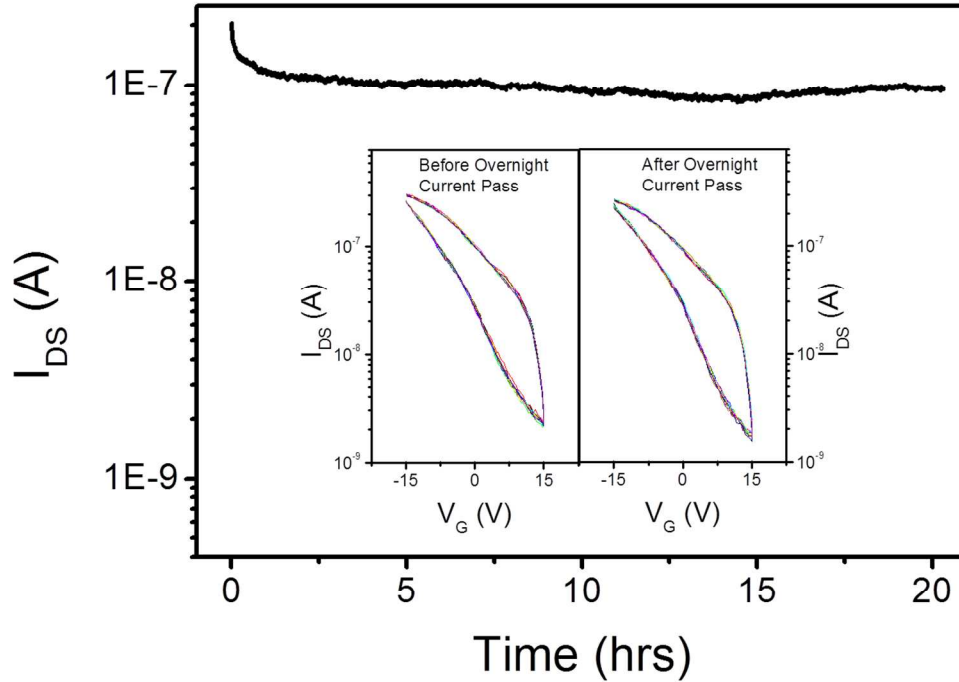

Figure S3. Time-dependence measurement of a nanosoldered device with $V_{DS} = 1$ V and $V_{GS} = -15$ V showing stable current over a 20-hour interval. The inset plots show consistent transfer curves before (left) and after (right) the 20-hour current flow treatment. Each plot is composed of 10 transfer curves measured consecutively.

For control experiments, CNT devices of similar network and crossbar geometries were used. These control devices were prepared in the same way; the devices were annealed at 600 K to remove oxygen molecules in vacuum,[7] treated with similar current flow methods but in the absence of precursors, and exposed back to air for sufficient time (over 24 hours) to assess any changes in their transfer characteristics. Figures S4a summarizes the degree of improvement in the I_{ON}/I_{OFF} ratio ($I_{ON}/I_{OFF,AFTER}$ / $I_{ON}/I_{OFF,BEFORE}$) for these devices, along with the devices nanosoldered with HfB_2 and Pd. As can be seen in the figure, the performance of control devices remained about the same or even degraded, possibly due to decreased channel and CNT-electrode contact resistances from the heat generated during the current passing through the device. The heat generated from this current anneal may cause the elimination of contaminants in CNTs and may also thermally anneal the contacts. The decreased channel and contact resistances can increase both I_{ON} and I_{OFF} and lower the overall I_{ON}/I_{OFF} ratio. The degree of decrease in these resistances may vary from device to device and from different batches of devices.

As noted in the main text, an improvement in the I_{ON}/I_{OFF} ratio of ~2.4 was observed in one of our control devices (indicated by green dotted circle in Figure S4a). Figure S4b shows an SEM image of this device. Note that during the control experiment, V_{GS} was set at 15 V and V_{DS} was applied from 5 V to 40 V for both current paths between Source 1 & Drain 1 and Source 2 & Drain 2. Figure S4c shows the transfer characteristic curve between Source 1 & Drain 1 before and after the control experiment. After noticing changes in the I_{ON}/I_{OFF} ratio, we put this device back into CVD chamber, and performed nanosoldering with the Pd precursor using the same conditions. Note that current was only passed between Source 2 & Drain 2 (electrodes false-colored in red in the SEM image), and no current was passed between Source 1 & Drain 1. Then the measurements were made again using Source 1 and Drain 1 electrodes. By doing so, we were able to nanosolder the junctions and improve the I_{ON}/I_{OFF} ratio by another factor of ~8.25 (green dotted circle near right edge of Figure S4a). For AFM analysis on this device, refer to Figure S5 in the next section.
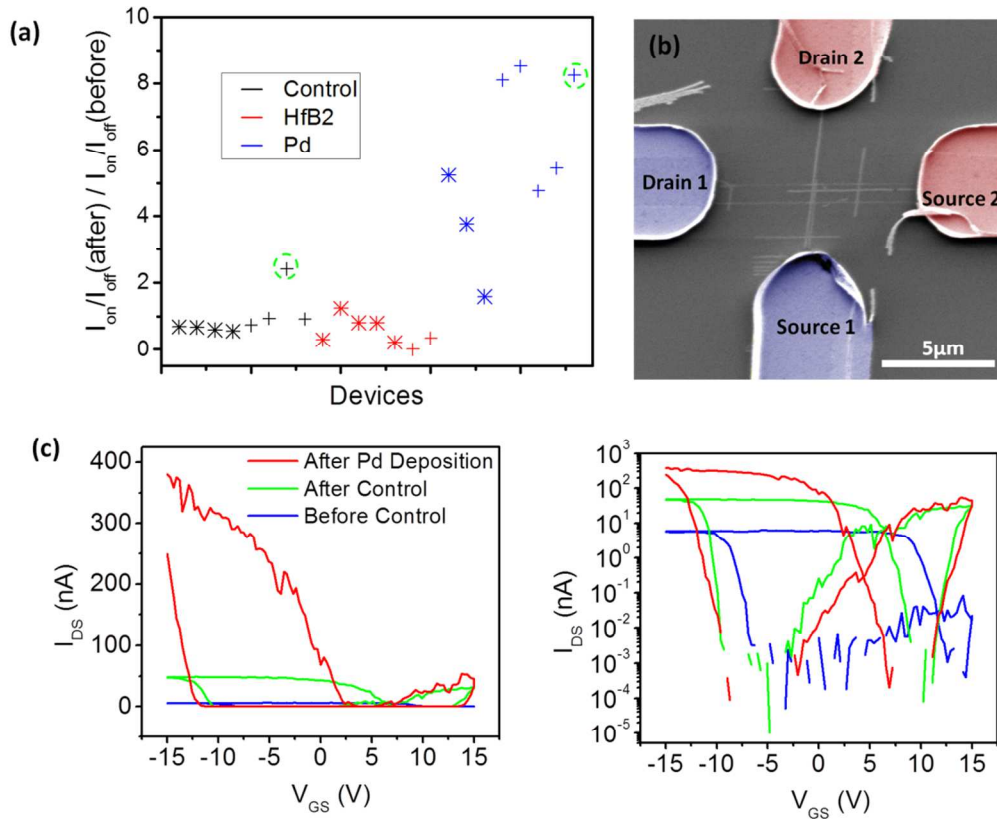

Figure S4. (a) Summary of improvement in I_{ON}/I_{OFF} ratios upon control experiment (black), HfB$_2$ deposition (red), and Pd deposition (blue). Points marked with * symbol corresponds to CNN devices and points marked with + symbol corresponds to CNT crossbar devices. **(b)** SEM image of a device indicated by green dotted circle in (a) before the control experiment. For the control experiment, current was passed between the source and drain of both red and blue electrodes. For Pd deposition, current was passed only between the red electrodes. **(c)** (Left) linear and (right) log scale transfer characteristics of the device in (b) measured between blue electrodes before and after the control experiment and Pd deposition.

4. **Verification of Pd Deposition on CNTs**

Atomic force microscope (AFM) images were collected using a Bruker Dimension IV AFM in tapping mode. The scan size was kept under 5 μm × 5 μm with a scan rate of 1 Hz. The resolution was 1024 × 1024. The drive amplitude and set point were carefully monitored to ensure good tracking of the surface. Figure S5a shows an SEM image of a CNT crossbar device before the control experiment and Pd deposition as discussed in the previous section. After the control experiment, current was passed between the red electrodes only and the electrical measurements were made using the blue electrodes (see Figure S4c). Figure S5b shows AFM images corresponding to the yellow dotted box in the SEM image before and after Pd deposition. The line scans along a CNT in dotted boxes (blue and red for before and after, respectively) show that sub-10 nm Pd particles were deposited at the junctions. We also note some Pd deposition along some other parts of CNTs, which may be defective sites.
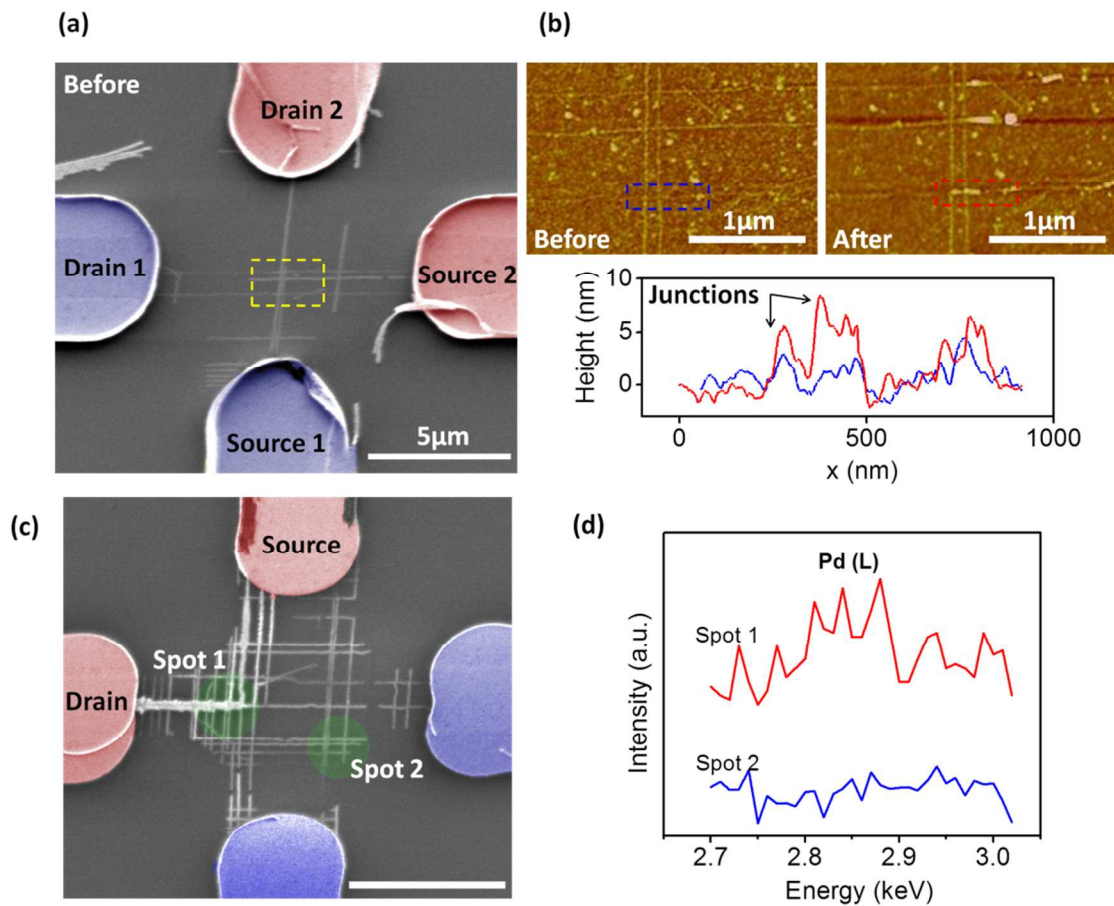

Figure S5. (a) SEM image of a device indicated by the green dotted circles in Figure S4a before the control experiment. **(b)** AFM images corresponding to the yellow dotted box in (a) before (left) and after (right) Pd deposition, showing Pd particles of sub-10 nm size at the junctions. The bottom plots show height profiles along the CNT shown in the dotted boxes in the AFM images. **(c)** SEM image of a crossbar CNT device after intentional overdeposition of Pd. Current was passed between the two red false-colored electrodes. Green circles indicate where the EDS spectra in (d) were obtained. Scale bar is 5 μm. **(d)** EDS spectra from Spot 1 (red) and Spot 2 (blue) verifying the presence of palladium.

In order to perform chemical analysis to verify the presence of Pd, EDS was performed on another device where high current was passed deliberately to deposit a large amount of Pd. Figure S5c shows an SEM image of such a crossbar CNT device after intentional overdeposition of Pd. Figure S5d shows EDS spectra from two different spots indicated by green circles in Figure S5c. EDS measurement from Spot 1 shows a Pd peak while the measurement from other parts of CNTs on the same device (Spot 2) does not show any noticeable Pd peak. The same measurement conditions were used for both cases and both plots are on the same scale.

5. Energy Dispersive X-ray Spectroscopy (EDS) for Boron

EDS analysis was performed using a FEI XL-30 SEM with field emission gun (FEG) source. Figure S6a shows SEM images of CNNs after HfB_2 deposition. Note that since boron is a light element, a CNT device with over-deposited HfB_2 is used for EDS. Spot 1 in the upper image of Figure S6a denotes the area where EDS spectrum (red curve) shown in Figure S6b was obtained. Spot 2 in the lower image of Figure S6a corresponds to CNN in the same device with no HfB_2 deposition, and the corresponding EDS spectrum (blue curve) is shown in Figure S6b. Note that the same acquisition conditions were used for both cases, and the two curves are on the same scale. The EDS data indicate that the deposited material indeed contains boron and the obtained boron spectrum is not simply from physisorbed precursor on the CNN.
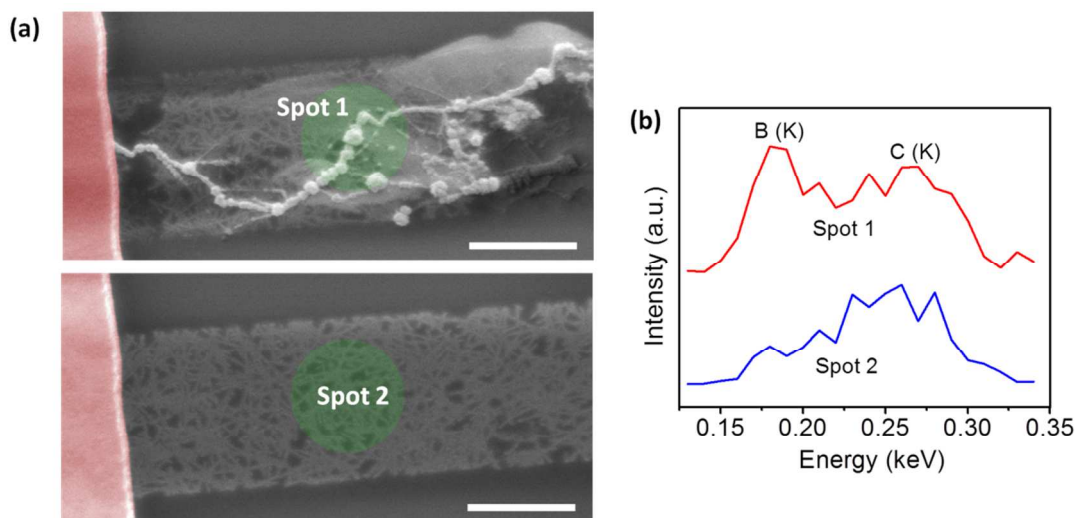

Figure S6. (a) SEM images of (top) CNT network (CNN) with over-deposited HfB_2 and (bottom) CNN in the same device with no deposition of HfB_2. Green circles indicate the spots where energy dispersive X-ray spectroscopy (EDS) spectra shown in (b) were obtained. Scale bar is 2 μm. **(b)** EDS spectrum from spot 1 (red) and spot 2 (blue) verifying the presence of boron.

References

(1)   Hur, S.-H.; Kocabas, C.; Gaur, A.; Park, O. O.; Shim, M.; Rogers, J. A. *J. Appl. Phys.* **2005**, *98*, 114302.

(2)   Xiao, J.; Dunham, S.; Liu, P.; Zhang, Y.; Kocabas, C.; Moh, L.; Huang, Y.; Hwang, K.-C.; Lu, C.; Huang, W.; Rogers, J. A. *Nano Lett.* **2009**, *9*, 4311–4319.

(3)   Kang, S. J.; Kocabas, C.; Kim, H.-S.; Cao, Q.; Meitl, M. A.; Khang, D.-Y.; Rogers, J. A. *Nano Lett.* **2007**, *7*, 3343–3348.

(4)   Borisenko, K. B.; Downs, A. J.; Robertson, H. E.; Rankin, D. W. H.; Tang, C. Y. *Dalton Trans.* **2004**, 967–970.

(5)   Tatsuno, Y.; Yoshida, T.; Otsuka, S.; Al-Salem, N.; Shaw, B. L. In *Inorganic Syntheses*; Shriver, D. F. Ed.; John Wiley & Sons, Inc.: Hoboken, NJ, 2007; Vol. 19, pp 220–223.

(6)   Timmermans, M. Y.; Estrada, D.; Nasibulin, A. G.; Wood, J. D.; Behnam, A.; Sun, D.; Ohno, Y.; Lyding, J. W.; Hassanien, A.; Pop, E.; Kauppinen, E. I. *Nano Res.* **2012**, *5*, 307–319.

(7)   Derycke, V.; Martel, R.; Appenzeller, J.; Avouris, P. *Appl. Phys. Lett.* **2002**, *80*, 2773–2775.